Scaling Laws for Deployable Mesh Reflector Antennas*

Jong-Eun Suh †, Sahangi P. Dassanayake‡
California Institute of Technology, Pasadena, California, 91125

Mark W. Thomson§
Tendeg LLC, Louisville, Colorado, 80027

Sergio Pellegrino¶
California Institute of Technology, Pasadena, California, 91125.

This paper begins with the formulation of a general, rapid design method for deployable mesh reflector antennas based on the AstroMesh architecture. This method is then used to obtain estimates of the total mass, stowed envelope size, and fundamental natural frequency of vibration for antennas with a range of aperture diameters and focal lengths, assuming an operational radio frequency of 10 GHz. A study of the scaling trends of this reflector design shows that the distribution of prestress in the inner tension structure has a major impact on the mass of the outer perimeter truss. Based on this result, a prestress optimization problem to design reflectors of minimum mass is formulated, and analytical scaling laws are obtained for the mass, stowed envelope and natural frequency of optimally prestressed reflectors with aperture diameters up to 200 m. It is then shown that aperture diameters of 70-100 m are at the limit of launchers that are currently available or under development. A semi-analytical homogenization model that accurately estimates the fundamental natural frequencies for batten-supported and free-free boundary conditions is also presented.

Main Nomenclature

A	=	cross-sectional area, m^2
A, B, D	=	stiffness coefficients, N/m, N, Nm
D	=	diameter of reflector, m
E	=	modulus, GPa
E^*	=	equivalent modulus, GPa
f	=	natural frequency, Hz

*An initial version of this paper was presented at SciTech Forum 2024, January 8-12, Orlando FL. AIAA 2024-2041.
†Postdoctoral Researcher, Graduate Aerospace Laboratories, AIAA Member. jsuh@caltech.edu
‡Graduate Student, Graduate Aerospace Laboratories, AIAA Student Member. sahangi.d@caltech.edu
§Chief Technology Officer.
¶Joyce and Kent Kresa Professor of Aerospace and Civil Engineering, Graduate Aerospace Laboratories, AIAA Fellow. sergiop@caltech.edu

F = focal length of reflector, m

g = maximum distance between perimeter truss and inner net, m

h = distance of joint bottom edges in folded configuration, m

H = length of batten, m

I = moment of inertia, kg/m^2

k = stiffness, Nm/rad

l = length of compression element, m

L = length of triangular facet, m

L_{ij} = length of member ij, m

L_{max} = maximum length of cable elements, m

m = mass, kg

n = number of subdivisions of faceted paraboloid

N = number of nodes connected to a free node

N = mid-plane stress resultant, N/m

n_c = number of boundary cables connected to a single batten

n_t = number of subdivisions in perimeter truss

p_{ij} = prestress in cable ij, N

P = perimeter, m

R = radius of spherical cap, m

s = edge height, m

S = distance between centers of longerons in type-2 joint, m

s_0 = vertical offset, m

x_i, y_i, z_i = coordinates of node i

t = thickness

T = matrix of tension tie force distributions, N

T_i = tension tie force applied to node i, N

T^k = k^{th} tension tie distribution, N

W = width of type-1 joint, m

α = angle between truss elements, rad

α = prestress coefficient

β = angle between boundary cables, rad

δ_{facet} = surface error due to faceting, mm

δ_{RMS} = surface root mean square error, mm

ϵ = strain component

λ = radio wave length, mm

ν = Poisson's ratio

ν^* = equivalent Poisson's ratio

σ = biaxial prestress of metallic mesh, N/m

Subscripts

eq = equivalent

n = cable net

s = stowed

SL = single layer

tt = tension ties

I. Introduction

Deployable mesh reflector antennas are widely used for communication and scientific observation. Commercial systems from several companies, including Astro Aerospace Northrop Grumman, L3 Harris and Tendeg, are currently available.

Initial concepts for deployable mesh reflectors were of the *umbrella* type [1] and consisted of gores of metallic wire mesh stretched across a set of parabolic ribs. The *Wrap-Rib Reflector* concept, with thin shell elastic ribs with a parabolic edge profile that could be wound around a central hub mechanism, was developed to achieve a shorter stowed volume [2]. However, achieving high surface accuracies was found to be challenging, particularly for antennas with larger aperture diameters. To address this challenge, the concept of a faceted reflective surface, formed by triangular mesh facets attached to a prestressed cable net forming a *Tension Truss*, was proposed [3, 4]. Building on this concept, Thomson and Hedgepeth developed the *AstroMesh Reflector* [5], in which a pair of doubly-curved cable nets are placed back-to-back in tension across the rim of a deployable perimeter truss.

This scalable concept has outperformed its predecessors in terms of surface accuracy, mass and packaged volume efficiency, and has been selected for many space missions [6–8] in sizes ranging from 3 m to 25 m. It has become a standard configuration for mesh reflectors, and many variants of the original implementation by Hedgepeth and Thomson have been proposed [9, 10].

Figure 1 shows the structural architecture of the AstroMesh reflector, consisting of three main components: the two cable nets, the metallic wire mesh, and the deployable perimeter truss. The metallic mesh is attached to the back side of the front cable net, to provide a radio frequency reflective surface that approximates to a paraboloid. The accuracy of the

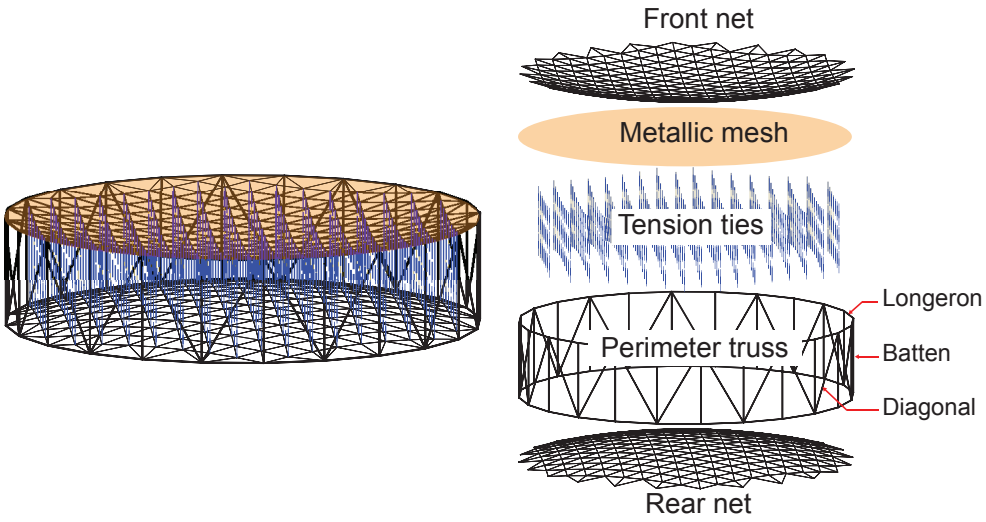

Fig. 1 Structural architecture of faceted deployable mesh reflector

approximation is determined by the size of the facets, which is related to the length of the cable elements forming the nets and hence to the density of the cable net nodes placed on the paraboloid. The front and rear nets are attached to the perimeter truss and are tensioned by ties stretched across corresponding node pairs on the two nets. The front and rear nets are identical and equally prestressed. The perimeter truss is composed of identical parallelogram repeating units, formed by two longerons (i.e., struts placed in the horizontal plane in Fig. 1), two battens (i.e., struts placed in a vertical plane in Fig. 1), and one diagonal that braces the parallelogram and is allowed to extend when the truss is folded.

High stiffness and thermal stability of the deployed and prestressed structure are achieved by selecting high-modulus tubes with near-zero coefficient of thermal expansion (CTE) for the truss, and thermally stable high-modulus tapes for the cable nets.

The reflective surface consists of triangular facets, whose size is determined by the operational radio frequency (RF) of the reflector. The size of the facets is determined such as to provide the required approximation to the paraboloid, measured by the surface RMS error, δ_{RMS}. Numerous form-finding studies for the cable nets have been conducted, to improve their surface accuracy and stability [11–15]. The dynamic behavior of the reflector is also a key part of the design process, to avoid coupling with the attitude control system of the spacecraft [16–19].

Basic metrics to evaluate deployable mesh reflectors for a specific application are the mass, stowed volume (which is related to accommodation in a launcher), and the natural frequency of vibration (related to the dynamic response of the reflector during operation). These metrics become particularly critical as the size of the reflector increases.

Despite the importance of such metrics, specifically for system-level studies of applications requiring large deployable mesh reflectors, no systematic study of their dependence on the aperture and focal length has been published. Most existing research has focused on improvements to the RF efficiency, but the mass and stowed volume improvements

have not been reported. An exception is a study of the increase in mass against the size of the reflector, for diameters up to 25 m, in Thomson [5]. Numerical and experimental studies of the dynamic behavior of mesh reflectors have also been published [17, 19], but high-fidelity numerical models and experimental models are not suitable for the analysis of extremely large reflectors, or for studies across a wide range of scales, because the number of elements in the structure quickly becomes very large. Therefore, the present study develops relatively coarse and simplified analysis methods with which key parameters of deployable reflectors can be estimated rather quickly. This study is not a replacement for the detailed design methods that have been presented elsewhere.

The foundation for the present scaling study is a general design methodology for faceted mesh reflector antennas. A simple approximation of the geometric error associated with faceting of the surface is used to estimate the maximum acceptable size of the facets and, based on this result, a basic design for the geometry of the facets is obtained. Then, the required connectivity between the edges of the faceted surface and the deployable perimeter truss is investigated, to ensure that the front cable net can be prestressed in a unique way (which requires the structure to be statically determinate) and has a unique shape (i.e., the structure is kinematically determinate). Once the geometry of the structure has been decided, the prestress distribution is optimized by varying the forces in the tension ties. Lastly, the components of the prestressed structure are sized to achieve appropriate margins against all relevant failure modes.

This methodology is used to design deployable center-fed mesh reflectors with an operational frequency of 10 GHz and with aperture diameters up to 200 m. Scaling laws for the mass, stowed volume, and natural frequency of vibration of these reflectors are obtained. Different boundary conditions that bound the behavior of larger reflectors on smaller spacecraft and vice versa are considered. Semi-analytical models are established to significantly reduce the computational effort in comparison to fully-detailed models.

The paper is organized as follows. Section II describes the geometric design of the reflector, and optimizes the prestress distribution in the structure. Section III derives the structural design. Section IV presents the scaling laws for the mass and the stowed envelope. Section V presents the scaling of the natural frequencies and the semi-analytical model to estimate the fundamental natural frequency. Finally, Section VI discusses the results and concludes the paper.

II. Geometry, Connectivity, and Prestress

A. Geometry, and design for kinematic and static determinacy

A paraboloidal reflective surface is required, to maximize the antenna's directivity [20]. Figure 2 shows a circular paraboloid with axis z, aperture diameter D, focal length F, edge height s, and and z-offset s_0. The equation of this surface is:

$$z = s_0 + \frac{x^2 + y^2}{4F} \tag{1}$$

An important geometric parameter is the ratio F/D. This study considers reflector designs with the three values

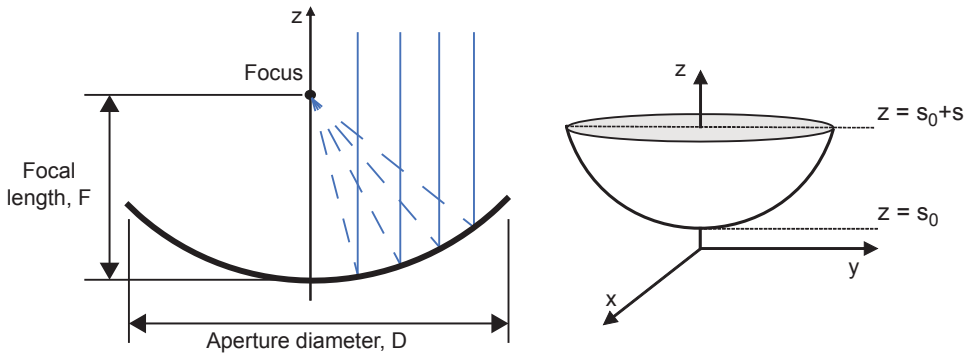

Fig. 2 Geometry of paraboloidal reflector

$F/D = 0.5, 0.7$, and 1.0.

For the purpose of designing a faceted surface, it is convenient to approximate the paraboloid with a surface of uniform curvature (sphere). The spherical cap that matches the paraboloidal cap of Fig. 2 at the apex and the edge has radius R given by [21]:

$$R = 2F + \frac{D^2}{32F} \tag{2}$$

The required size of the triangles is estimated by considering the geometric deviation between a spherical surface of radius R and an equilateral triangle of size L, with vertices lying on the curved surface. The root-mean-square error is given by [22]:

$$\delta_{facet} = \frac{L^2}{8\sqrt{15}R} \tag{3}$$

and this relationship can be used to estimate the required facet size L for given R and F/D. When a tessellation of equilateral triangles of side length L and lying in the x, y plane is vertically projected onto a paraboloid, the projected facets become increasingly elongated away from the z-axis. However, this error is small for relatively flat reflectors and small L/D.

This study considers geometric faceting as the only source of error, neglecting other error sources, such as thermal distortions, spillover, aperture taper, cross polarization, etc. Therefore, the RMS surface error is set equal to the faceting error in Eq. (3), i.e. $\delta_{RMS} = \delta_{facet}$. For a reflector operating at 10 GHz, the error is set equal to $\lambda/50 = 0.6$ mm and the maximum allowable facet size is then obtained from Eqs. (2) and (3). Note that the lengths in Eq. 3 are not the unstressed lengths of the cable net elements, but include the elastic stretching due to the prestress.

Figure 3(a) shows the variation of the facet size for different values of F/D. Larger facets are acceptable for higher values of F/D, which correspond to shallower and hence less curved reflectors, for the same aperture diameter. In general, the maximum size of the facets increases proportionally to $\sqrt{D}$.

Figure 3(b) shows the net configuration. Once the facet size has been decided, for a given aperture and F/D, the

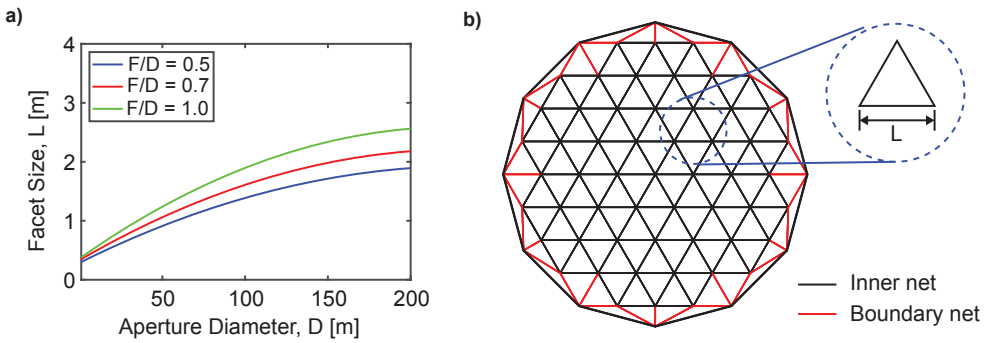

Fig. 3 Faceting of paraboloidal surface: a) variation of facet size with diameter, and b) schematic layout of net

number of subdivisions, n, of the hexagonal tessellation is calculated as:

$$n = 0.5D/L \tag{4}$$

The front and rear nets of the reflector include a set of inner cables forming the regular tessellation depicted with black solid lines in Fig. 3(b)) and the outer cables connecting the triangles to the perimeter truss, depicted with red lines in Fig. 3(b). The two colors define the *inner net* and the *boundary net*, respectively. The nodes of the inner net, which are connected by the tension ties between the front and rear nets, are called *free nodes*.

Even though the geometry of the inner nets is unique, for a given facet size, the design of the boundary nets can still vary, depending on the number of bays in the perimeter truss and the connections to the inner nets. Figure 4 shows three different net designs with the same edge subdivision ($n = 7$). Note that in the design of the boundary cables, it is assumed that each node of the perimeter truss is connected to the same number of free nodes, n_c. The number of subdivisions in one-sixth of the perimeter truss is denoted by n_t. A similar approach was previously adopted in [23].

In order to design reflectors with a unique shape and prestress distribution, the degrees of kinematic and static determinacy of the reflector were investigated by analyzing the pin-jointed bar model of each cable net, as shown for example in Fig. 5, using the extended Maxwell's equation and the rank of the equilibrium matrix [24–26]. This analysis leads to the conclusion that these properties depend upon the net geometry. For example, the net configuration in Fig. 4(a) contains non-triangular facets and hence the pin-jointed model is kinematically indeterminate. The structure is statically indeterminate when there are cross wires in the boundary net, as in Fig. 4(b). Only the configurations consisting of triangular facets without cross wires (e.g., the configuration shown in Fig. 4(c)) are both kinematically and statically determinate, and are therefore chosen for the structural architecture of the reflector. For reflectors designed in this way, the number of subdivisions of the hexagonal tessellation is related to the number of free nodes connected to

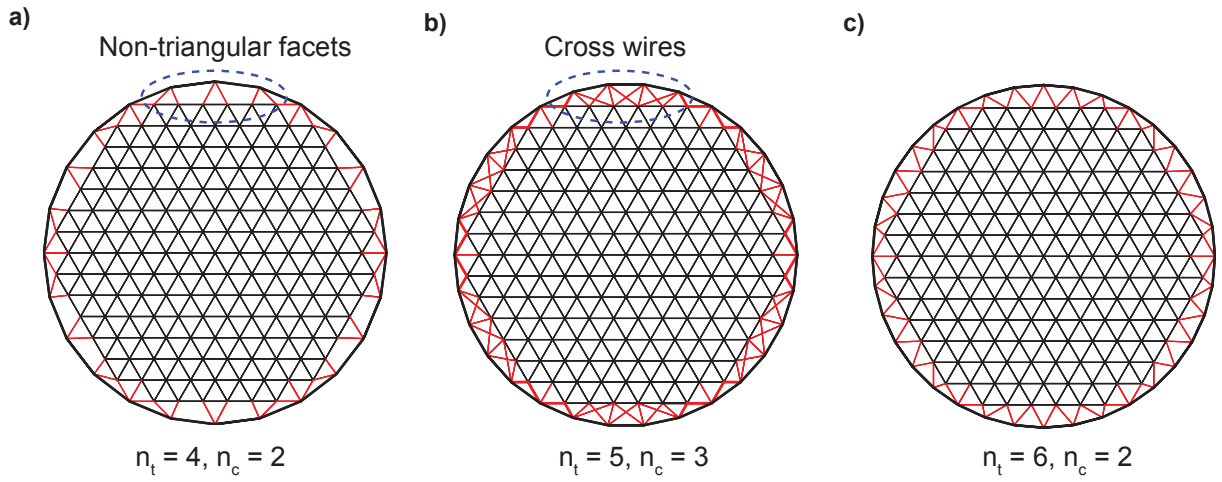

Fig. 4 Three different net configurations with a) non-triangular facets, b) cross wires, and c) complete triangular tessellation

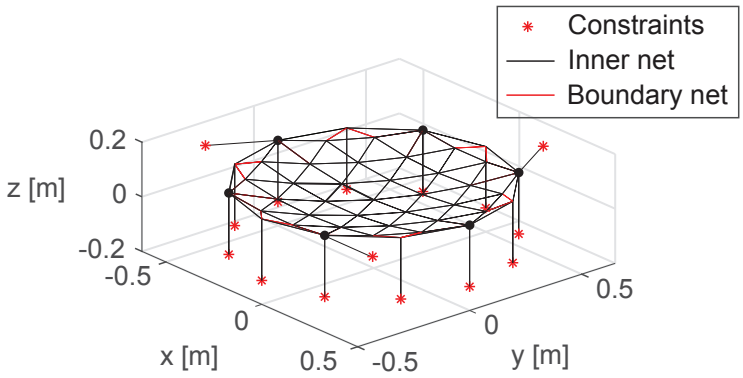

Fig. 5 Pin-jointed bar model of front net for $n = 3, n_c = 2, n_t = 2$

each node of the perimeter truss and the subdivision of the perimeter truss by the relationship:

$$n - 2 = (n_t - 1)\,(n_c - 1) \tag{5}$$

In the present study, the perimeter truss has been designed to have half the density of the net. Hence, a single batten supports three free nodes with boundary cables (i.e., $n_c = 3$ in Eq. (5). The lengths of the longerons, battens, and diagonals were determined based on the designed net geometry.

B. Prestress optimization of cable nets

Optimizing the prestress of the reflector is very important because the prestress is directly related to the structural mass. A higher prestress results in higher loading levels for the structural elements which will therefore have to be increased in size, leading to heavier mass. Importantly, this effect is most significant for the elements of the structure

that are put under compression by the prestress, i.e. the elements of the perimeter truss. It will be shown that, for large diameter reflectors, designs based on optimal prestress are significantly lighter than reflectors based on non-optimized prestress.

Because the structure is statically determinate by design, for any given geometry of the nets, once the tension tie forces are applied to the nets, the prestress distribution is uniquely determined by the equilibrium equations for the nodes. For example, the equation of equilibrium in the x-direction for each free node, i, connected to N nodes, j, is (see [26] for more details):

$$\sum_{j}^{N} \frac{x_i - x_j}{L_{ij}} p_{ij} = t_{i,x} \tag{6}$$

where,

L_{ij} is the length of cable ij, and hence $L_{ij} = \sqrt{(x_i - x_j)^2 + (y_i - y_j)^2 + (z_i - z_j)^2}$;

p_{ij} is the tension in cable ij;

$t_{i,x}$ is the component of the tension tie force applied to node i, in the x-direction.

The simplest approach is to compute the prestress corresponding to a single value of the tension tie forces at all free nodes. However, the result is that several cables near the transition between the inner and boundary nets end up under compression (in reality they would be slack). An entirely tensile distribution of prestress can be obtained by increasing to a suitable value $\alpha > 1$ the tie forces applied at the free nodes of the transition region.

Figure 6 (a) shows the distribution of prestress in the cable net for $D = 200$ m, $F/D = 1.0$, and $\alpha = 1.7$. This value was determined by trial and error.

This method of applying two distinct tie forces also resulted in a lower overall mass of the structure, which suggested that the overall structural mass may be further reduced through a more formal study of general prestress distributions, which required formulating an optimization problem. Theoretically, different tie forces could be applied at each free node but this approach is not practical. To simplify the practical implementation, six-fold rotational symmetry of the hexagonal tessellation was assumed. Hence, the number of distinct tension tie forces was set equal to the number of *rings*, see Fig. 7, in the tessellation, i.e., $n + 1$. This approach can be extended to offset reflectors, for which the assumption of six-fold symmetry is not valid, by considering larger sets of cable tensions, for each ring of tension tie forces.

A basis for the independent tension tie forces, T, was considered by computing the distribution T^k that corresponds to unit tension tie forces at all of the free nodes on ring k, and zero forces at all other free nodes. Denoting by P^k the

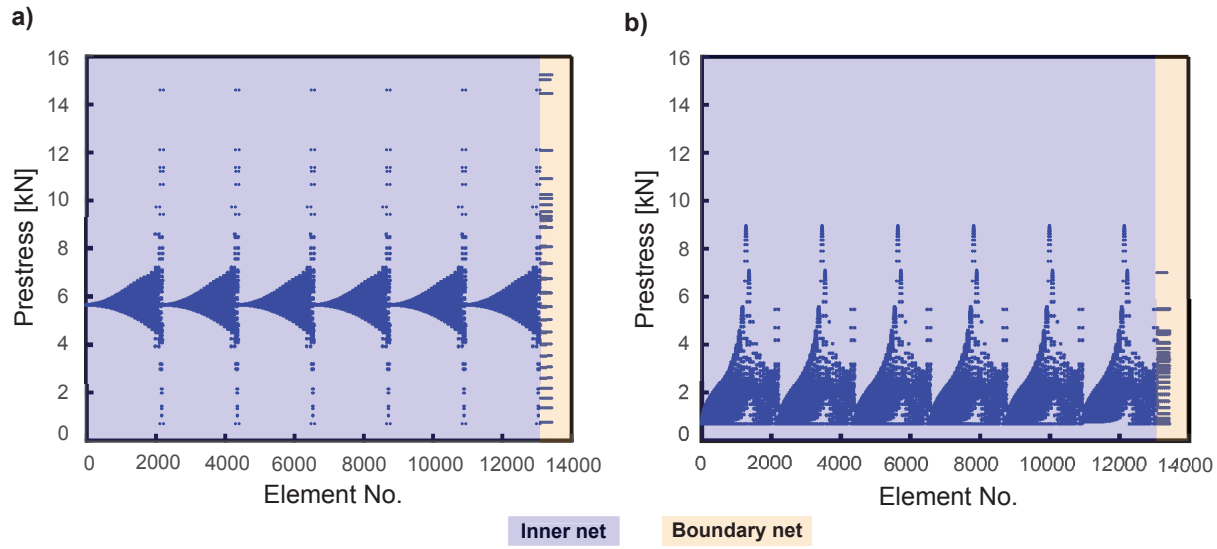

Fig. 6 Comparison of cable prestress distributions for $D = 200$ m, $F/D = 1.0$ corresponding to (a) 2 distinct tension tie forces, and (b) *(n + 1)* rings of tension tie forces

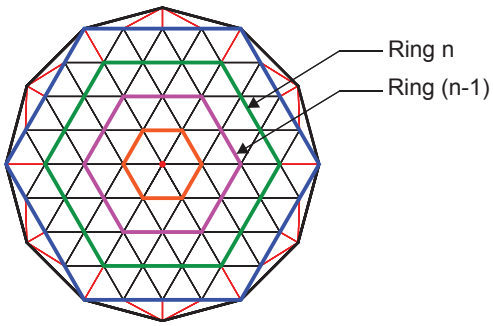

Fig. 7 Definition of *rings* in inner net

prestress distribution in the cable net in equilibrium with T^k, the following two matrices are defined:

$$T = \left[\underline{T}^1 \ \underline{T}^2 \ \cdots \ \underline{T}^{n+1}\right] \tag{7a}$$

$$P = \left[\underline{P}^1 \ \underline{P}^2 \ \cdots \ \underline{P}^{n+1}\right] \tag{7b}$$

Then, a general tie force distribution is $T\alpha$ and the corresponding set of of cable tensions p_{ij} is given by $P\alpha$, with coefficients $\alpha_k > 0$ to ensure that all tension tie forces are positive.

A further constraint is that a sufficient level of pretension should be applied to all cables, to keep them both under tension and sufficiently straight when they are loaded by the prestressed metallic mesh. The minimum required tension is [27]:

$$p_{ij} \geq 10\sigma L_{max} \tag{8}$$

where,

σ is the biaxial prestress in the metallic mesh;

L_{max} is the maximum cable length in the net.

Different objective functions were considered for the optimization and two metrics, the maximum compressive forces in the perimeter truss and the range of cable tensions $\frac{(P)_{max}}{(P)_{min}}$ were evaluated after minimizing each objective function. Both of these metrics directly contribute to the overall structural mass of the reflector, as discussed in Sections III and IV. The results of this analysis, presented in Table 1, show that all variants considered lead to improvements in both metrics. Also, the same reduction of 32% in mass with a 41% reduction in the range of cable tensions is achieved with five different objective functions. One of these five objective functions, the average batten force in the perimeter truss was selected as objective function for the prestress optimization.

Table 1 Comparison of Objective Functions for $D = 200$ m, $F/D = 1.0$

Objective Function	$\frac{P_{max}}{P_{min}}$	Maximum Compressive Force (kN)	Mass (kg)
RMS Deviation of cable tensions	10.546	145.25	13,259
Range of cable tensions	10.027	138.71	13,039
Maximum longeron force	12.816	138.42	13,030
Average longeron force	12.816	138.42	13,030
Maximum batten force	12.816	138.42	13,030
Average batten force	12.816	138.42	13,030
Sum of tension tie forces	12.816	138.42	13,030
Solution with two distinct tension tie forces	21.775	379.47	19,061

It is interesting to visually compare the cable force distribution for the initial (two tension tie force) solution, Fig. 6(a), vs. the optimal distribution obtained in this way, Fig. 6(b), for $\sigma = 5.0$ N/m. This figure shows that the majority of cable tensions is significantly lower.

III. Structural Design

A. Metallic mesh and cable nets design

Knitted gold-plated molybdenum wire mesh with areal density $\rho_{mesh} = 0.025$ kg/m^2 was selected for the reflector design, and a biaxial prestress $\sigma = 5$ N/m was assumed.

The front and rear nets are formed of thin CFRP strips of M55J carbon fiber in a thermoplastic matrix. The density of this composite material is $\rho_n = 1,786$ kg/m^3 and its longitudinal modulus $E_n = 325.4$ GPa. A rectangular cross-section, 6 mm wide and 150 μm thick, was selected for reflectors of all apertures. The closest distance between the front and rear nets (i.e., $2s_0$) was held constant at 0.1 m for all of the reflector designs considered in this study, as larger values would increase the length of all battens.

The pretension of the cable nets was obtained from the optimization described in Section II. Based on the net prestress, the corresponding compression forces in the perimeter truss were obtained from the equilibrium equations of the truss joints. The prestress analysis results for reflectors with apertures $D = 10$ m, 100 m, and 200 m are summarized in Table 2.

Table 2 Prestress range (Nets: tension. Truss: compression)

	Nets (kN)		Truss (kN)	
D(m)	Inner net	Boundary net	Longerons (kN)	Battens (kN)
10	0.042 ~ 0.114	0.045 ~ 0.139	0.947 ~ 1.072	0.046 ~ 0.052
100	0.357 ~ 2.160	0.357 ~ 1.838	25.794 ~ 29.182	0.484 ~ 0.567
200	0.700 ~ 8.967	0.700 ~ 7.000	120.220 ~ 138.420	1.545 ~ 1.859

B. Perimeter truss design

Due to the high compressive forces applied to the perimeter truss, tubes with circular cross-section were chosen for all members. A minimum diameter of 5 mm was assumed to avoid impractically small tubes.

Assuming pin-ended conditions, the global critical buckling load, P_{cr}, of a thin-walled circular tube of length l, cross-sectional radius r and thickness t, is given by:

$$P_{cr} = \frac{\pi^3 r^3 t E}{l^2} \tag{9}$$

where E is the longitudinal modulus.

Given that the longerons are subjected to the largest compressive force, they were sized first. Their thickness was set to 1.0 mm and the radius was determined using Eq. 9 with a load margin of 2. Next, the battens and the diagonals were designed to have the same cross-sectional radius as the longerons, to enable a simpler and lighter design of the joints of the perimeter truss. The minimum thickness of the battens was set at 1.25 mm, and it was confirmed that the buckling load from Eq. 9 is larger than the compressive force applied to the battens.

Theoretically, the diagonals are not subjected to any compression, although they are loaded in bending during deployment. Therefore, the size of the diagonals was simply set to be the same as the longerons, but with a thickness of 0.75 mm.

The radius and thickness of the longerons, battens, and diagonals for reflectors with apertures $D = 10$ m, 100 m, 200 m are presented in Table 3.

C. Joint design

The mass of the joints of the perimeter truss was estimated, for a general aperture D and different values of F/D, through a parametric design process purely based on geometry. There are two different types of joints, Type 1 is

Table 3 Size of perimeter truss members, for $F/D = 1.0$

D(m)	Radius of Longeron/ Batten/Diagonal (mm)	Thickness of Longeron (mm)	Thickness of Batten (mm)	Thickness of Diagonal (mm)
10	6.145	1.00	1.25	0.75
100	45.434	1.00	1.25	0.75
200	94.102	1.00	1.25	0.75

connected to 5 members (longeron, diagonal, batten, diagonal, longeron), and Type 2 is connected to 3 members (longeron, batten, longeron). See Fig. 8(a).

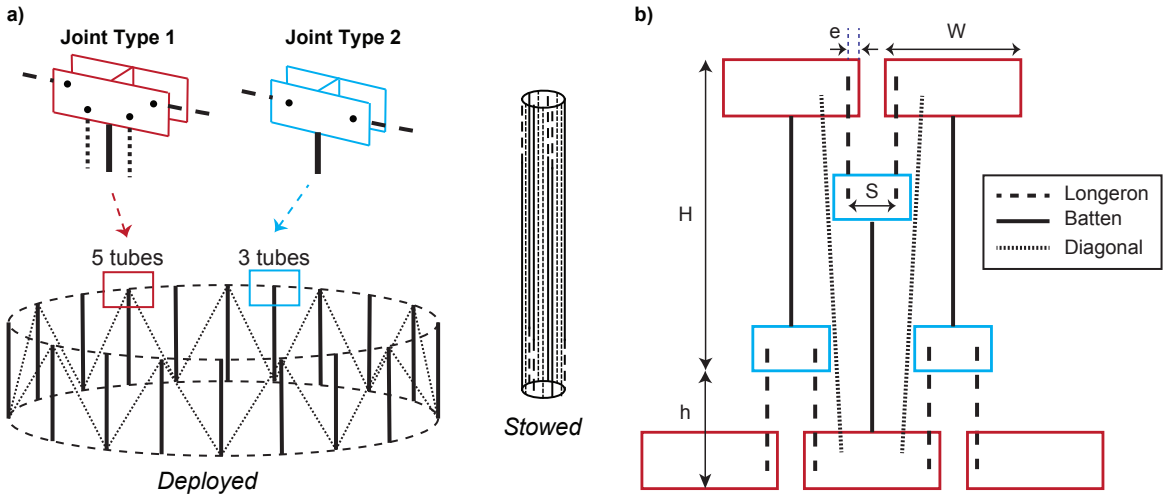

Fig. 8 Perimeter truss: a) fully deployed and stowed configurations, and b) relative position of members in stowed configuration.

The general arrangement of both joint types is shown in Fig. 8 (see also the supplementary material); two parallel plates made of CFRP (with the same material properties as the struts and cable net elements) are connected at the center to a plate made of 6061 Aluminum alloy ($\rho_{Al} = 2700$ kg/m^3, $E_{Al} = 69$ GPa). This central plate is firmly attached to the batten. The longerons and the diagonals are attached to appropriate locations on the side plates via 6061 Aluminum alloy sleeves and steel pins and bolts ($\rho_S = 7800$ kg/m^3, $E_S = 210$ GPa) that allow rotation for stowage/deployment.

Once the longeron size had been determined, as discussed in Section IIIB, the position of the pins attaching the longerons and diagonals to the plates was determined by considering the clearance required to allow the unimpeded rotation of these members about the pins. The plate and sleeve thicknesses were determined by considering the allowable margins for hole bearing failure at the pin attachments (~ thickness $\geq 3\times$ hole diameter [28]). The mass of the joints designed using the procedure described above, for apertures of $D = 1$ m, 10 m, 100 m, and 200 m, and $F/D = 1.0$, is presented in Table 4).

Table 4 Joint masses for $F/D = 1.0$

	Joint Mass (g)	
D(m)	Type-1	Type 2
1	18.0	10.3
10	45.2	23.2
100	2,272	1,076
200	10,780	5,284

IV. Scaling of Mass and Stowed Envelope

A. Estimating mass and stowed dimensions

The total mass of the reflector was estimated by adding the contributions of the cable nets (m_n), metallic mesh (m_{mesh}), perimeter truss (m_{truss}), tension ties (m_{tt}), joints (m_j), and deployment actuators (m_{dep}):

$$m_{total} = m_n + m_{mesh} + m_{truss} + m_{tt} + m_j + m_{dep} \tag{10}$$

The mass of each component was calculated based on the structural design described in Section III. The mass of the cable net was calculated from the cross-sectional area of the strips, multiplied by the total length of the strips and the density. The mass of the metallic mesh was calculated assuming that the complete surface of the front net is covered by the mesh. Hence, the area of the paraboloid surface was multiplied by the areal density of the mesh. The mass of the perimeter truss was calculated based on the structural design of the longeron, batten, and diagonal members described in Section III. The mass of the joints was estimated by linear interpolation of the results in Table 4. The mass of the tension ties and the seams in the mesh, m_{tt}, was assumed to be equal to $2 \times m_{mesh}$. The mass of the deployment actuators was assumed to be 10% of the total mass of the reflector.

The stowed envelope of the reflector was assumed to be of cylindrical shape, as shown in Fig. 8. The diameter of this cylinder is determined by the perimeter of the stowed configuration, which is the configuration in which there is contact between adjacent joints. The height of the cylinder is defined by the length of the battens and longerons. Figure 8(b) is a schematic drawing showing the relative positions of the truss members on the joints and the design parameters determining the stowed dimensions of the structure.

In Fig. 8(b), H is the total height of the perimeter truss when fully deployed. The distance between the bottom edges of type-1 and type-2 joints in the folded configuration is defined as h. The length of a type-1 joint, the distance between the center of the hinge of the longeron and the edge of the joint, and the distance between the centers of the hinges of the longerons in a type-2 joint are defined as W, e, and S, respectively. Hence, the perimeter of the stowed reflector, P_s can be calculated from:

$$P_s = (W + S - 2e) \times (0.5n_t) \tag{11}$$

and then the diameter in the stowed configuration is given by $D_s = P_s/\pi$. The height of the stowed configuration is $H + h$.

B. Mass and stowed dimensions results

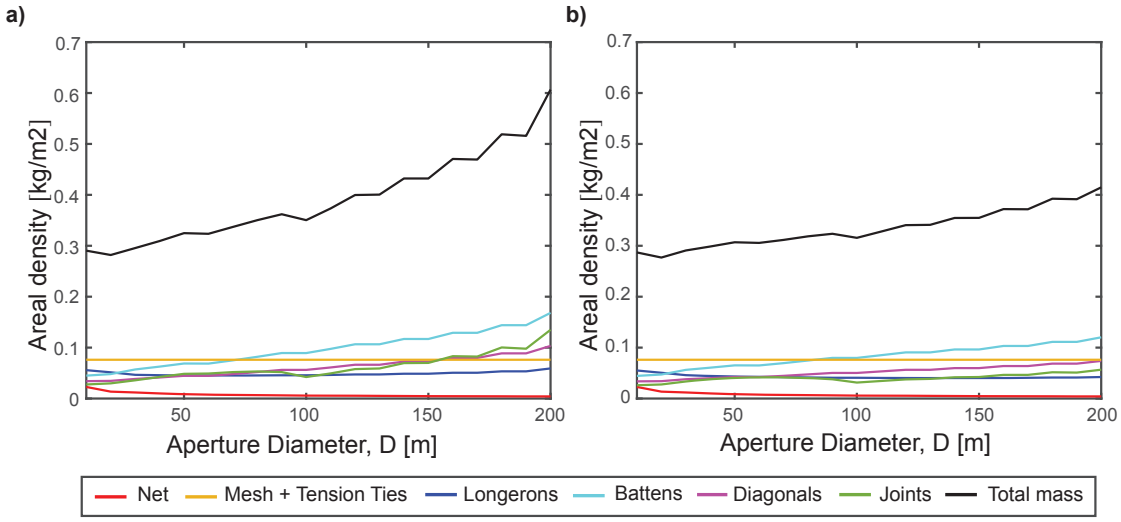

Fig. 9 Areal density of reflector components ($F/D = 1.0$): a) non-optimal prestress design, and b) optimal prestress design

The variation of the equivalent areal density of the various reflector components has been plotted in Fig. 9 versus the aperture, for $F/D = 1.0$. Comparison of the two graphs clearly shows the superior mass efficiency of the optimal prestress distribution. For the case of two distinct tension tie forces, Fig. 9(a), the areal density increases nonlinearly with the diameter of the reflector, mainly due to the rapidly increasing mass of the battens and diagonals in the perimeter truss. With the optimal prestress distribution, plotted in Fig. 9(b), the compressive forces in the perimeter truss are smaller than the two-tension design. The difference between the two approaches is small for apertures below 50 m, but becomes ever larger, as the lower prestress of the truss reduces the size of its members and achieves almost a one-third reduction in areal density, for aperture diameters of around 200 m.

The overall mass, stowed diameter and height of the reflector are presented in Fig. 10 for $F/D = 1.0$, for the diameter range 10 m to 200 m.

Two launch vehicles, the Falcon Heavy [29] and the Starship [30], were selected to establish the availability of launchers for mesh reflectors with a large aperture. In Fig. 10(b) and (c), the pink and blue solid lines represent the payload limits for Falcon Heavy and Starship, respectively. Given the maximum payload mass to geostationary transfer orbit (GTO) is 26, 700 kg for the Falcon Heavy [29], even the largest reflectors considered in the present study are well below this limit. However, the launch envelope restrictions are much more stringent, particularly the stowed diameter requirement. Reflectors with aperture diameter larger than 70 m cannot be accommodated in the Falcon Heavy, and

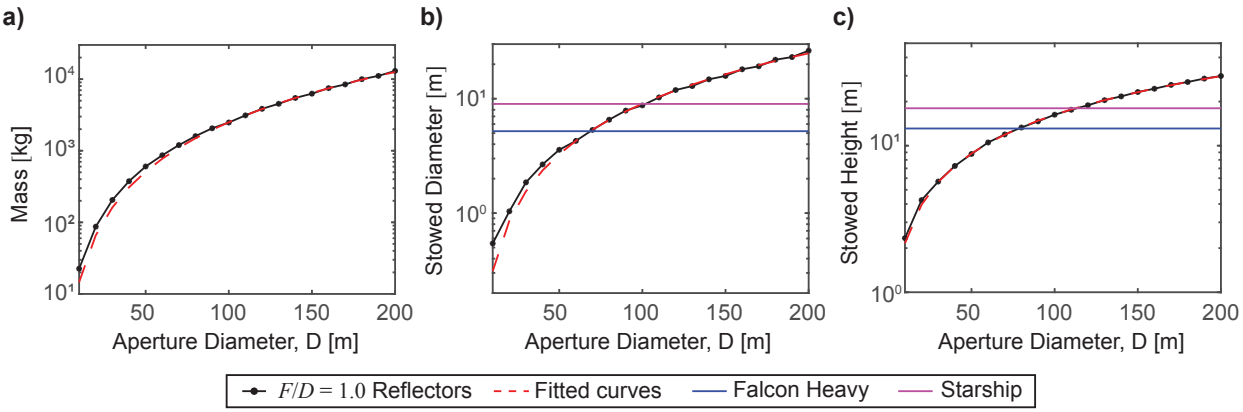

Fig. 10 Scaling of reflectors with $F/D = 1.0$: a) total mass, b) stowed diameter, and c) stowed height

100 m is the aperture limit for launch in the Starship. Mass and stowed volume scaling plots for different F/D values are provided in the supplementary material.

The present scaling study has provided the valuable insight that the launch of deployable mesh reflectors is restricted first by the diameter of the stowed reflector and second by its height, whereas the launch mass limits are much higher. Since it has been shown that extremely large scale space-borne deployable reflector antennas are not feasible, there is a clear opportunity to pursue alternative structure-building strategies, such as on-orbit assembly, to overcome the volumetric payload restrictions currently imposed by launch vehicles [31, 32].

C. Analytical scaling laws

The results presented in the previous section can be used to establish analytical scaling laws for the mass and the stowed envelope of deployable mesh reflectors designed according to the optimized prestress distribution, presented in Section IIB.

To derive a mass scaling equation, the reflector components were grouped into three separate categories that scale in an equal manner, based on the structural design procedure; the mass of the perimeter truss including the joints, the mass of the cable net, and the mass of the mesh and tension ties. Each category of mass was expressed as a separate power function of D, as outlined in Fig. 11. The coefficients of the power law terms, $C1$, $C3$ and $C5$ were scaled to reflect the mass of the deployment actuators, setting them at 10% of the total mass.

The resulting scaling law, for the mass (in kg) of reflectors with $F/D = 1.0$ is therefore:

$$m_{total} = 0.022D^{2.452} + 0.054D^{1.492} + 0.067D^{2} \tag{12}$$

The detailed mass of reflectors with $F/D = 1.0$ has been plotted together with this analytical expression in Fig. 10(a). It can be seen that Eq. 12 follows the total mass of the reflector very closely.

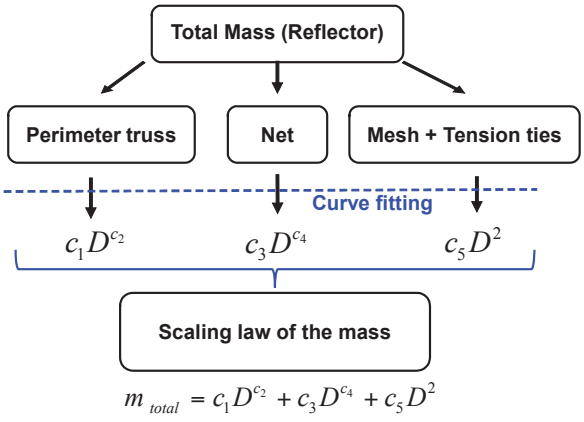

Fig. 11 Process of establishing scaling law for the total mass

The situation is different when the stowed diameter and height of the deployable reflector are considered. In this case, the contribution of the cable nets, mesh and tensions ties are negligible, as the stowed envelope size is dominated by the members of the perimeter truss and the joints. Therefore, single-term power functions were chosen to derive the following analytical expressions for the diameter and height:

$$D_s = 0.011 D^{1.464} \tag{13}$$

$$H_s = 0.286 D^{0.877} \tag{14}$$

which have been plotted in Fig. 10(b) and (c).

Whereas the scaling laws of the mass and stowed envelope presented in this section are valid for $F/D = 1.0$ designs, additional scaling studies for $F/D = 0.5, 0.7$ are presented in the supplementary material.

V. Scaling of Natural Frequencies of Vibration

A. Finite element model and boundary conditions

A geometrically nonlinear, high-fidelity finite element model was set up in Abaqus 2017 to investigate the natural frequencies of vibration of deployable mesh reflectors. The model included all of the structural elements, individually modeled as described next. The front and rear nets were modeled with truss elements (T3D2), each edge of a triangular facet consisting of a single truss element. The members of the perimeter truss, longerons, battens, and diagonals were modeled with 20 beam elements (B31). The connections between adjacent elements were modeled as pin joints, which allow relative rotation. The metallic mesh was modeled as point masses equally distributed over the nodes of the front net. The mass of the joints and the deployment actuators was modeled as point masses connected to the joints of the

perimeter truss. A pre-defined stress field was assigned, based on the prestress level for each structural component obtained from the optimization process in Section II.B. Tension tie forces were applied to the inner nodes of the front and rear nets. The model was set up in the operational geometric configuration of the reflector, with the prestress also applied in this configuration, to avoid significant geometry changes during the geometrically nonlinear iteration to reach the prestressed equilibrium configuration.

First, a static equilibrium analysis was performed for the structure under a pre-defined stress field as well as the tension tie forces, and the deformed geometry and stiffness of the reflector were obtained. A modal analysis was then carried out for the structure subjected to the boundary conditions of interest and in the equilibrium configuration, to obtain the natural frequencies and corresponding mode shapes.

Two different boundary conditions were considered. The first boundary condition assumed that the reflector is connected to a massive spacecraft through a prime batten that avoids interference with the deployment of the perimeter truss. The prime batten, shown in Fig. 12(a), is attached to the perimeter truss through three joints in the upper layer of the truss, and one joint in the lower layer. In Abaqus, this batten-supported boundary condition was realized by restricting 6 DoFs (degrees-of-freedom) at four joints of the perimeter truss as shown in Fig. 12(b).

The second boundary condition is free-free and captures the increasing dominance of the reflector's dynamics as the size of the reflector increases.

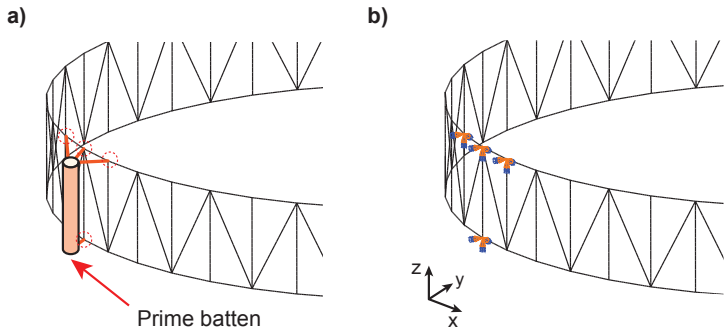

Fig. 12 Batten-supported boundary condition: a) prime batten, and b) boundary conditions in finite element model

B. Natural frequencies and mode shapes

Key results of the finite element modal analysis are summarized in Fig. 13 for $F/D = 1.0$. The log-log trend for the lowest natural frequencies, see Fig. 13(a), is a straight line of negative slope, indicating a negative power law decrease with the diameter of the reflector. Typical mode shapes are shown in Fig. 13(b) and Fig. 13(c), respectively for batten-supported and free-free boundary conditions.

For the batten-supported boundary condition, the two dominant mode shapes are a lateral mode, where the structure rotates around the prime batten, and a vertical mode where the structure moves mostly in the z-direction, as a cantilever

attached to the prime batten and vibrating up and down. The natural frequencies for these modes are rather close. For $D < 25$ m the fundamental mode is vertical and for $D > 25$ m the fundamental mode is lateral.

For the free-free boundary condition the fundamental mode vibration is saddle-like, as shown in Fig. 13(c). The fundamental frequency for this boundary condition is an order of magnitude higher than for the batten-supported boundary condition.

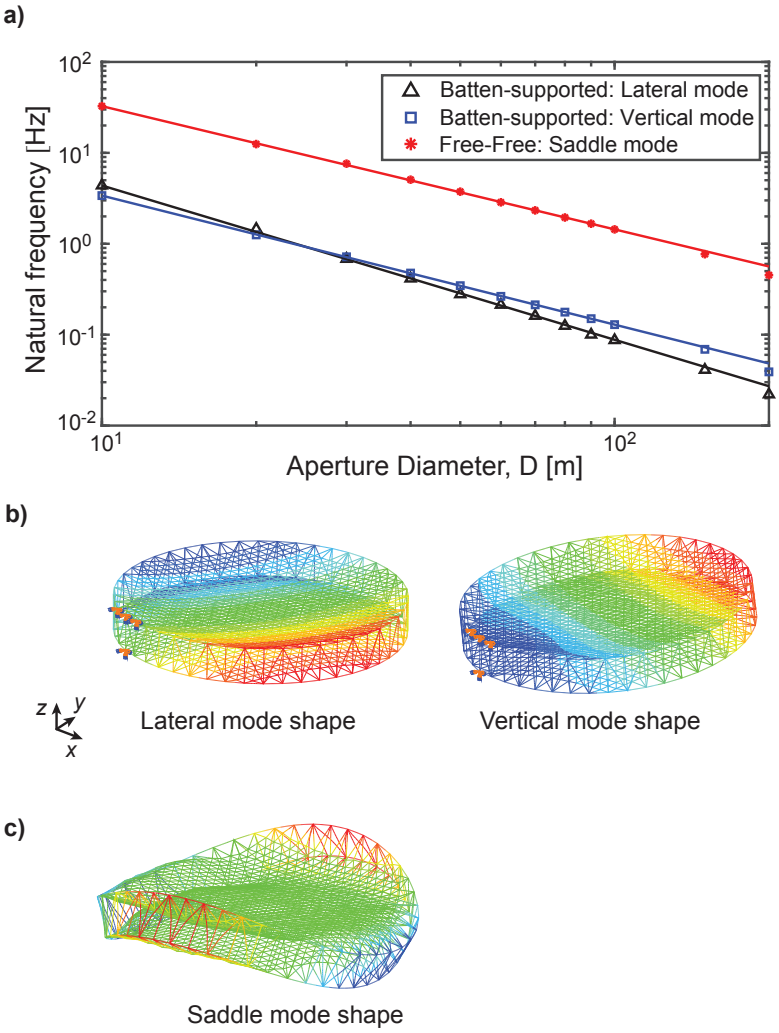

Fig. 13 Natural frequencies and mode shapes: a) frequency trends, b) first two mode shapes for prime-batten support c) first mode shape for free-free condition

The results of the detailed modal analysis have been fitted with power laws, Fig. 13(a), which represent the high-fidelity simulation results with RMS error values of 0.014, 0.003, and 0.116 Hz, respectively for lateral, vertical,

and saddle mode frequencies. The corresponding analytical expressions (in Hz) are:

$$
\begin{aligned}
f_{lateral} &= 217.2 \times D^{-1.699} \\
f_{vertical} &= 88.43 \times D^{-1.419} \\
f_{saddle} &= 738.1 \times D^{-1.357}
\end{aligned}
\tag{15}
$$

Note that these scaling laws are valid for reflectors with $F/D = 1.0$. The scaling laws for $F/D = 0.5, 0.7$ are presented in the supplementary material.

C. Semi-analytical models for fundamental frequencies

While the high-fidelity modal analysis provides accurate estimates of the natural frequencies and mode shapes for reflectors of any aperture, in the case of larger reflectors the required computations become very lengthy due to the increasing number of structural elements in the model. A semi-analytical model can provide much faster and also rather accurate estimates.

Figure 14 outlines the modeling approach. The basic idea is to homogenize the mesh reflector to an edge-stiffened circular elastic plate. The cable nets are modeled by a flat continuum disk with equivalent stiffness. The perimeter truss is homogenized to an equivalent hoop, attached to the outer edge of the disk. This scheme can be applied to all mode shapes, although the details of the model are different. The derivation of the semi-analytical model is presented for the lateral mode shape, which corresponds to the lowest frequency for reflectors with larger apertures and batten-supported boundary conditions, and for the saddle mode.

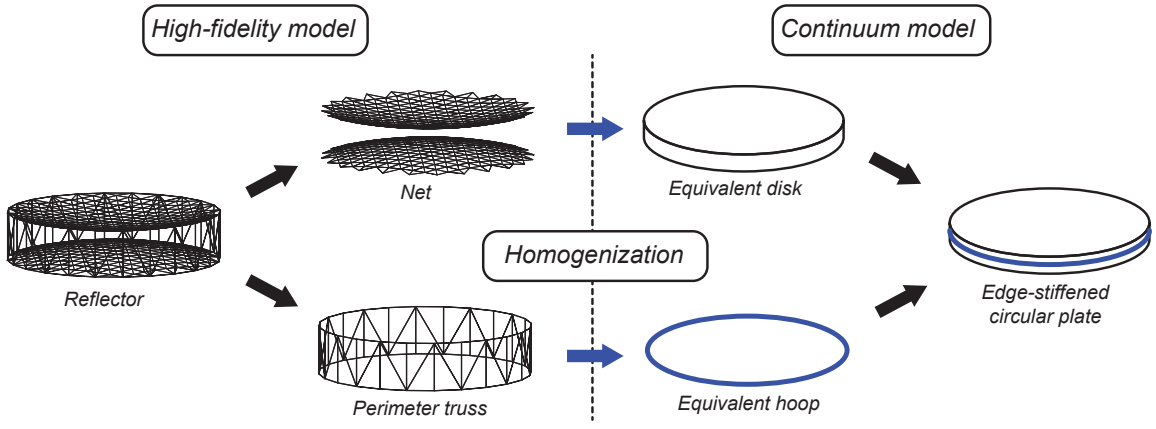

Fig. 14 Semi-analytical modeling scheme

The lateral mode shape for the batten-supported boundary condition is an in-plane vibration mode, where the entire reflector rotates against the three joints of the perimeter truss that are constrained by the prime batten and are assumed

to be rigidly fixed. This vibration mode can be represented by the 1-DoF mass-spring system in Fig. 15(a), where m_{eq} is the total mass and I_{eq} is the moment of inertia of the reflector around a horizontal axis through the center of of mass. The stiffness, k_{eq}, of the torsional spring attached to the rigid bar of length $D/2$ is obtained from an elastic analysis of an equivalent edge-stiffened continuum disk subject to the same boundary conditions as the reflector structure, and loaded by an external couple, as shown. The three supports of the disk represent the constraints applied by the prime batten to the upper ring of longerons.

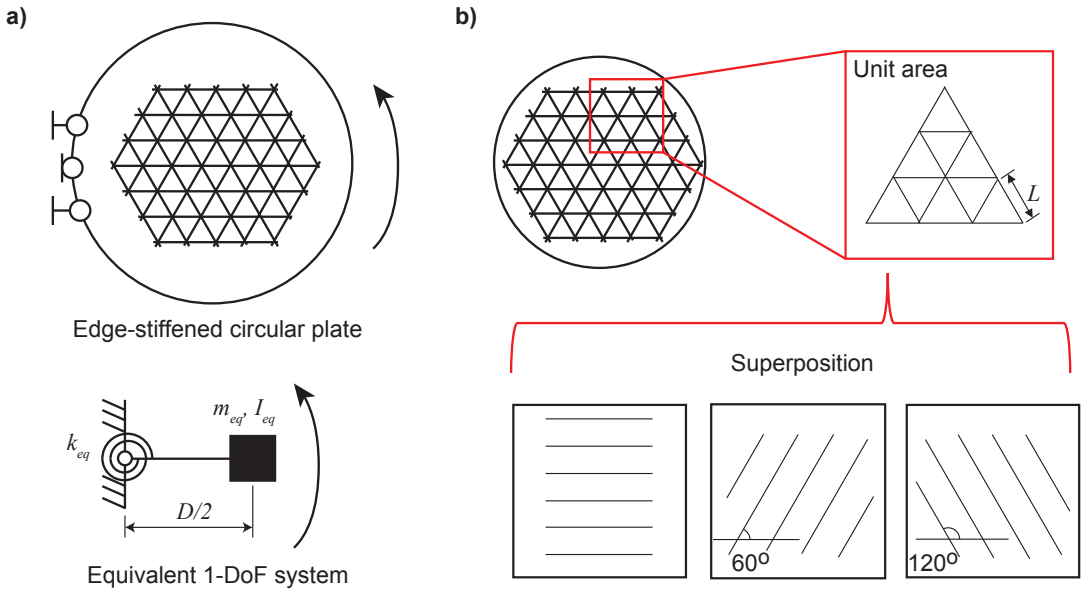

Fig. 15 Semi-analytical model to estimate lateral mode: a) 1-DoF model, and b) homogenization of the net

Figure 15(b) summarizes the stiffness homogenization of the front net. The rear net is not considered, because the single constraint applied by the prime batten leaves the lower ring of longerons effectively free to rotate.

It should be noted that, first, the truss elements in the front net are assumed to be coplanar (i.e., the curved shape of the net is neglected) and, second, the net is composed of a uniform tessellation of equilateral triangles with edge length L.

The homogenized stiffness matrix for a single-layer truss tessellation, A_{SL}, is calculated by superposition of three parallel trusses [26], Fig. 15(b), with modulus E_n and cross-sectional area A_n:

$$A_{SL} = \frac{3\sqrt{3}E_n A_n}{4L} \tag{16}$$

The equivalent continuum Young's modulus, E^*, and Poisson's ratio, ν^*, are (see the Appendix for details):

$$E^* = \frac{2\sqrt{3}E_n A_n}{3t_n L}, \quad \nu^* = \frac{1}{3} \tag{17}$$

Considering that the longerons are placed along the perimeter of the front net, a circular hoop having the same cross-section as the longerons is attached to the edge of the homogenized disk, thus completing the semi-analytical model of the edge-stiffened disk.

The equivalent torsional stiffness, k_{eq}, is estimated by carrying out an elastic stiffness analysis of the edge-stiffened disk, measuring the rotation of the equivalent model under a given moment. The moment of inertia is the sum of I_{eq} and the parallel axis contribution. Hence, the natural frequency of the mesh reflector is calculated from:

$$f_{lateral} = 2\pi\sqrt{\frac{k_{eq}}{m_{eq}D^2/4 + I_{eq}}} \tag{18}$$

Figure 16 compares the natural frequencies obtained from the finite element analysis with the proposed semi-analytical approach. The lateral mode frequencies are in good agreement with the results from the high-fidelity model. The results, also presented in Table 3, show an error reaching 22.27% for the largest diameter. This error is mainly due to the difference in stiffness between the actual cable net and the homogenized disk.

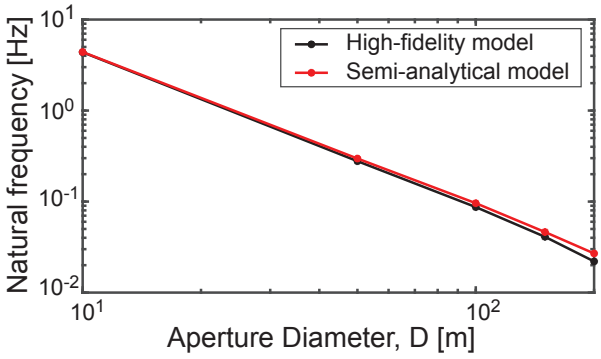

Fig. 16 Natural frequency corresponding to lateral mode

Table 5 Natural frequency of lateral mode (high-fidelity model vs. semi-analytical model)

	Natural frequency (Hz)		
D(m)	High-fidelity model	Semi-analytical model	Error (%)
10	4.346	4.371	0.58
50	0.276	0.294	6.54
100	0.086	0.095	10.30
150	0.041	0.046	12.39
200	0.022	0.027	22.27

In contrast to the lateral vibration mode, the free-free saddle mode involves an out-of-plane motion and hence the bending stiffness of the equivalent model is required to estimate k_{eq}. In this case, the homogenization scheme was modified to estimate the bending stiffness of the prestressed nets as well as the contribution of the perimeter truss.

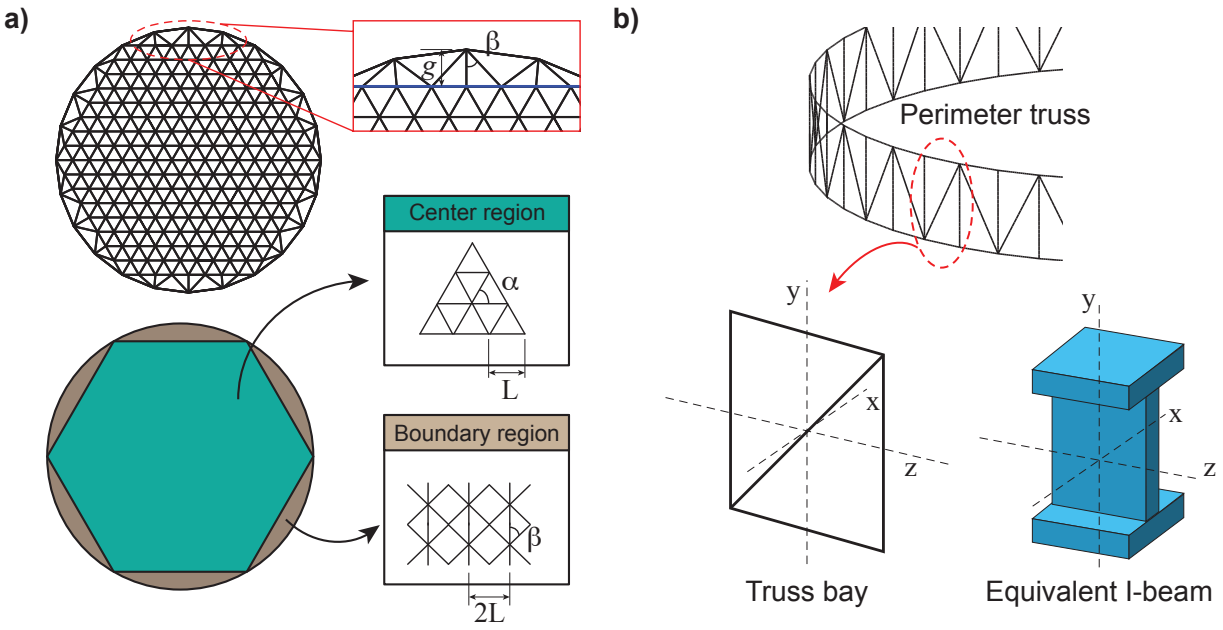

Fig. 17 Semi-analytical model for free-free saddle mode: homogenization of a) net, and b) perimeter truss

The bending and torsional stiffnesses of the continuum model were obtained by multiplying the in-plane continuum stiffness of each net by the square of the local distance between the nets [26].

This model can be refined by allowing for the fact that the x, y plane projections of the triangles that connect the inner net to the perimeter truss are not equilateral. The in-plane stiffness of the central hexagon, composed of identical equilateral triangles, was A_{SL} as before. The region bounded by the perimeter truss and the hexagonal region at the center has a coarser cable pattern, as shown in Fig. 17(a). The equivalent material properties of the disk were obtained considering these distinct cable patterns, allowing for the different angles and distances between the cables in the boundary region. The angle between the cables, β, has the expression:

$$\beta = \tan^{-1}\left(\frac{L}{g}\right) = \tan^{-1}\left(\frac{4\left(2+\sqrt{3}\right)L}{D}\right) \tag{19}$$

The ABD stiffness matrix of the equivalent disk was then obtained following the derivation for double-layer space frames in [26]. Given that the front and rear nets are identical, $A \approx 2A_{SL}$ and $D \approx A_{SL}(2z)^2$, where z is the distance between the two nets. Then, substituting Eq. 1 and $r^2 = x^2 + y^2$, the ABD matrix at a radial distance r from the axis paraboloid is expressed as:

$$ABD\,(r) = \begin{bmatrix} A & B \\ B^T & D\,(r) \end{bmatrix} = \begin{bmatrix} 2A_{SL} & 0 \\ 0 & \left(2s_0 + \frac{r^2}{2F}\right)A_{SL} \end{bmatrix} \tag{20}$$

where the B matrix is zero, for symmetry.

The perimeter truss is formed by identical bays, Fig. 17(b). In the proposed semi-analytical model for the saddle vibration mode, the perimeter truss was homogenized to an equivalent I-beam, with the same second moment of area as a bay, for all axes. Again, the equivalent hoop was attached to the edge of the equivalent disk and a modal analysis was conducted on this continuum model, with Abaqus 2017.

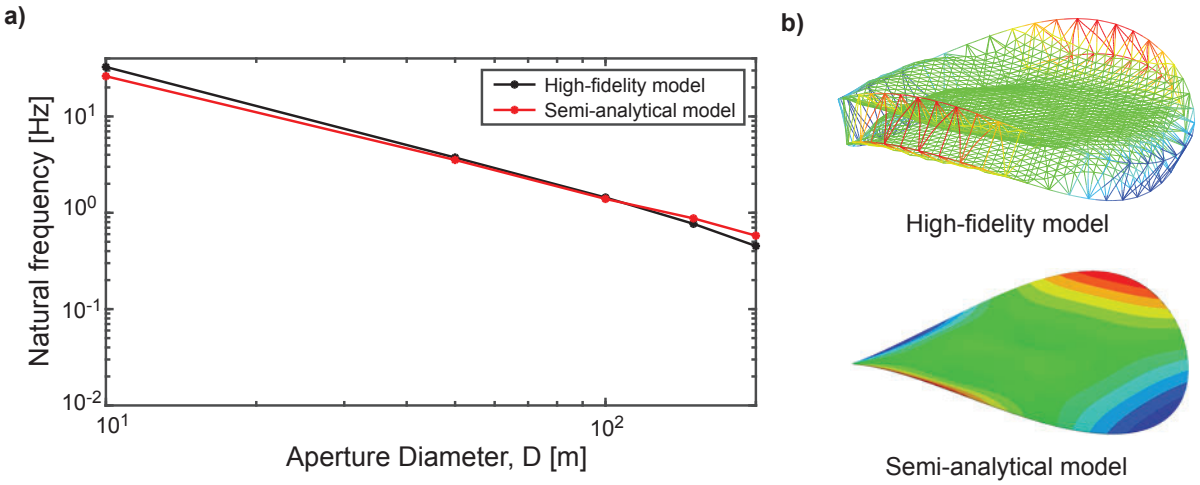

Fig. 18 Natural frequency of free-free saddle mode: a) frequency comparison, and b) mode shape comparison

Figure 18(a) compares the saddle mode frequencies (free-free boundary condition) obtained by the high-fidelity simulation with the results from the semi-analytical model. The corresponding numerical values are compared in Table 6 . The mode shape obtained from the semi-analytical model is in good qualitative agreement with the shape resulting from the finite element modal analysis, as shown in Fig. 18(b).

Table 6 Natural frequency of saddle mode (high-fidelity model vs. semi-analytical model)

	Natural frequency (Hz)		
D (m)	High-fidelity model	Semi-analytical model	Error (%)
10	32.473	26.153	19.85
50	3.702	3.535	5.56
100	1.430	1.393	3.26
150	0.764	0.875	13.93
200	0.452	0.579	28.10

VI. Discussion and Conclusion

A general design method for deployable mesh reflector antennas based on the AstroMesh structural architecture has been presented. This reflector structure consists of two cable nets attached to a deployable perimeter truss along

the edges, with a prestressed metallic mesh attached to the front cable net, forming a faceted reflective surface that approximates to a paraboloid.

The length of the cable net elements was estimated by considering the root-mean-square error associated with faceting the required paraboloidal surface. A faceting error of $\lambda/50$ was considered acceptable, corresponding to δ_{RMS} = 0.6 mm at 10 GHz (λ = 30 mm). General design equations (Eqs 2 -3) were provided to calculate the cable lengths for given λ, F, and D. The design of the boundary nets, which connect the regularly tessellated inner nets to the perimeter truss, has identified a specific layout, called a complete triangular tessellation, in which the corners of the hexagonal tessellation forming the inner nets are directly connected to the perimeter truss, and any additional edge joints of the hexagonal tessellation are connected to two joints of the perimeter truss. This arrangement results in a statically and kinematically determinate pin-jointed structural model for the cable net, which guarantees a uniquely determined state of prestress and a unique geometry.

The front and rear nets have identical geometry and are equally loaded. They are tensioned by tension ties stretched across corresponding node pairs.

The tension tie forces have to be such that all cable elements are in a state of pretension. Among the many ways of meeting this requirement, it has been shown that the particular choice of the tension tie forces has a major impact on the level of compressive prestress in the perimeter truss, which in turn has a major impact on its total design mass. A method of optimizing the tension tie force distribution, grouping the tension ties into rings of equal value, has been formulated, and objective functions that lead to the design of reflectors of minimum mass have been presented. The minimum level of prestress is such that every cable net element has a tension greater or equal than 10 times the required operational prestress of the metallic mesh multiplied by the length of the element (Eq. 8). Setting the minimum prestress of the cable net in this way prevents excessive bowing of the cables when they are transversely loaded by the prestressed mesh.

The deployable perimeter truss is composed of identical parallelogram-shaped bays. Each bay consists of two longerons, two battens (shared with adjacent bays), and a bracing diagonal that is allowed to extend when the bay is folded.

Once the geometry, connectivity and state of prestress of the cable nets have been selected, together with the prestress of the perimeter truss, the structural design can be rapidly completed by sizing the various components. The cable net tapes are lightly loaded, and hence their size was chosen on the basis of the minimal practical width and thickness. Next, the deployable perimeter truss was designed, choosing circular tubes of equal outer diameter throughout, in order to simplify the design of the joints. The dimensions of the most loaded elements of the perimeter truss, the longerons, were chosen first, using a multiplier of 2 for the critical elastic buckling limit. A minimum diameter of 5 mm was imposed and the thickness was set at 1 mm. Next, the thickness of the battens was set, assuming a minimal value of 1.25 mm and again ensuring a multiplier of 2 for the critical elastic buckling limit. Finally, the diagonals, which are unloaded when the reflector structure is symmetrically prestressed, were set to have a thickness of 0.75 mm.

The joints of the perimeter truss consist of two parallel, flat plates perpendicular to a central plate aligned with the battens. The size of the parallel plates is such that the hinged longerons and diagonals can rotate without interference when the structure is folded. The geometry of the joint design is determined by the cross-sectional diameter of the tubes, selected in the previous step of the structural design, and their thickness is such as to allow the necessary margin on bearing failure.

Once the structural design of the reflector had been completed, as described above, its total mass, stowed volume and fundamental natural frequency of vibration were estimated, and the whole analysis was repeated for reflectors of many aperture diameters, focal lengths. The radio frequency was set at 10 GHz in the present study, but an extension to other radio frequencies , and also to other geometric configurations of the reflector would be straightforward and, indeed, would be a useful extension of the present work.

The results of the present study show that the areal density of prestress-optimized reflectors remains practically constant when the aperture diameter is increased, whereas non-optimized designs lead to an areal density that increases with the diameter.

Analytical scaling laws have been obtained for the mass, stowed envelope and natural frequency. Launch envelope requirements are identified as the limiting factor for aperture diameters over 70 m. A semi-analytical homogenization model has been presented, to accurately capture their mode shapes and estimate the fundamental natural frequencies for batten-supported and free-free boundary conditions.

An important conclusion from the present study is that the largest possible aperture diameter is constrained by the stowed envelope of the structure rather than its mass, for deployable mesh reflectors.

Appendix: Homogenized stiffness matrix of parallel tessellation

The equivalent in-plane stiffness matrix for equally-spaced parallel truss elements at an angle α to the x-axis has the expression [26]:

$$\begin{bmatrix} N_x \\ N_y \\ N_{xy} \end{bmatrix} = \frac{EA}{l} \begin{bmatrix} \cos^4\alpha & \sin^2\alpha\cos^2\alpha & \sin\alpha\cos^3\alpha \\ \sin^2\alpha\cos^2\alpha & \sin^4\alpha & \sin^3\alpha\cos\alpha \\ \sin\alpha\cos^3\alpha & \sin^3\alpha\cos\alpha & \sin^2\alpha\cos^2\alpha \end{bmatrix} \begin{bmatrix} \varepsilon_x \\ \varepsilon_y \\ \gamma_{xy} \end{bmatrix} \tag{21}$$

where, E, A, and l are the Young's modulus, cross-sectional area, and the distance between the elements, respectively. N_x, N_y, N_{xy} are the force per unit width stress resultants and $\epsilon_x, \epsilon_y, \gamma_{xy}$ are the in-plane strain components.

The homogenized in-plane stiffness matrix of the complete truss tessellation is then calculated by adding the stiffness matrix for each set of parallel elements.

For example, the truss tessellation formed of equilateral triangles in Fig. 17(b), is subdivided into three sets of parallel trusses with inclination angle, $\alpha = 0°$, $60°$, and $120°$. Note that the distance between two parallel trusses is

$\sqrt{3}L/2$, while Young's modulus and cross-section of the truss are defined as E_n, and A_n, respectively. By using Eq. (21), the constituent equation for the truss tessellation becomes:

$$\begin{bmatrix} N_x \\ N_y \\ N_{xy} \end{bmatrix} = \frac{3\sqrt{3}E_nA_n}{4L} \begin{bmatrix} 1 & 1/3 & 0 \\ 1/3 & 1 & 0 \\ 0 & 0 & 1/3 \end{bmatrix} \begin{bmatrix} \varepsilon_x \\ \varepsilon_y \\ \gamma_{xy} \end{bmatrix} \tag{22}$$

Funding Sources

This research was funded by the DARPA NOM4D program directed by Dr Andrew Detor, under grant HR001122C0054.

References

[1] Roederer, A. G., and Rahmat-Samii, Y., "Unfurlable satellite antennas a review," Annales des Télécommunications, Vol. 44, 1989.

[2] Russell, R.A., Campbell, T.G., and Freeland, R.E., "A technology development program for large space antennas," NASA-TM-81902, 1980.

[3] Miura, K. "Research and development of the tension truss antenna," IAF-87-317, 1987.

[4] Miura, K., and Miyazaki, Y., "Concept of the tension truss antenna," AIAA Journal, Vol. 28, No. 6, 1990, pp. 1098–1104. https://doi.org/10.2514/3.25172

[5] Thomson, M. W., "The Astromesh deployable reflector," IEEE Antennas and Propagation Society International Symposium. 1999 Digest. Held in conjunction with: USNC/URSI National Radio Science Meeting (Cat. No. 99CH37010), Vol. 3, IEEE, 1999, pp. 1516–1519. https://doi.org/10.1109/APS.1999.838231

[6] Thomson, M., "AstroMesh deployable reflectors for ku and ka band commercial satellites," 20th AIAA international communication satellite systems conference and exhibit, 2002, p. 2032. https://doi.org/10.2514/6.2002-2032

[7] Smith, T., Lee, B., Semler, D., and Chae, D., "A large S-band antenna for a mobile satellite," Space 2004 Conference and Exhibit, 2004, p. 6120. https://doi.org/10.2514/6.2004-6120

[8] Entekhabi, D., Njoku, E. G., O'Neill, P. E., Kellogg, K. H., Crow, W. T., Edelstein, W. N., Entin, J. K., Goodman, S. D., Jackson, T. J., Johnson, J., et al., "The soil moisture active passive (SMAP) mission," Proceedings of the IEEE, Vol. 98, No. 5, 2010, pp. 704–716. https://doi.org/10.1109/JPROC.2010.2043918

[9] Scialino, L., Ihle, A.,Migliorelli, M., Gatti, N., Datashvili, L., van 't Klooster, N., and Santiago-Prowald, J., "Large deployable reflectors for telecom and earth observation applications," CEAS Space Journal, Vol. 5, No. 3-4, 2013, pp. 125–146. https://doi.org/10.1007/s12567-013-0044-7

[10] Datashvili, L., Endler, S., Wei, B., Baier, H., Langer, H., Friemel, M., Tsignadze, N., and Santiago-Prowald, J., "Study of mechanical architectures of large deployable space antenna apertures: from design to tests," CEAS Space Journal, Vol. 5, No. 3-4, 2013, pp. 169–184. https://doi.org/10.1007/s12567-013-0050-9

[11] Yang, D., Zhang, Y., Yang, G., and Du, J., "Least-squares minimization of boundary cable tension ratios for mesh reflectors," AIAA Journal, Vol. 56, No. 2, 2018, pp. 883–888. https://doi.org/10.1016/j.engstruct.2021.112722

[12] Yuan, S. and Yang, B., " The fixed nodal position method for form finding of high-precision lightweight truss structures," International Journal of Solids and Structures, Vol. 161, 2019, pp.82-95. https://doi.org/10.1016/j.ijsolstr.2018.11.011

[13] Zhang, S., Zhang, S., Zhang, Y., and Ye, J., "Force density sensitivity form-finding design method for cable-mesh reflector antennas considering interactive effects between cable network and supporting truss," Engineering Structures, Vol. 244, 2021, p. 112722. https://doi.org/10.1016/j.engstruct.2021.112722

[14] Li, T., Jiang, J., Deng, H., Lin, Z., and Wang, Z., "Form-finding methods for deployable mesh reflector antennas," Chinese Journal of Aeronautics, Vol. 26, No. 5, 2013, pp. 1276–1282. https://doi.org/10.1016/j.cja.2013.04.062

[15] Yang, D., Zhang, Y., Li, P., and Du, J., "Numerical form-finding method for large mesh reflectors with elastic rim trusses," Acta Astronautica, Vol. 147, 2018, pp. 241–250. https://doi.org/10.1016/j.actaastro.2018.04.007

[16] Li, P., Liu, C., Tian, Q., Hu, H., and Song, Y., "Dynamics of a deployable mesh reflector of satellite antenna: parallel computation and deployment simulation," Journal of Computational and Nonlinear Dynamics, Vol. 11, No. 6, 2016. https://doi.org/10.1115/1.4033657

[17] Li, P., Liu, C., Tian, Q., Hu, H., and Song, Y., "Dynamics of a deployable mesh reflector of satellite antenna: form-finding and modal analysis," Journal of Computational and Nonlinear Dynamics, Vol. 11, No. 4, 2016. https://doi.org/10.1115/1.4033440

[18] Morterolle, S., Maurin, B., Dube, J.-F., Averseng, J., and Quirant, J., "Modal behavior of a new large reflector conceptual design," Aerospace Science and Technology, Vol. 42, 2015, pp. 74–79. https://doi.org/10.1016/j.ast.2015.01.002

[19] Siriguleng, B., Zhang, W., Liu, T., and Liu, Y., "Vibration modal experiments and modal interactions of a large space deployable antenna with carbon fiber material and ring-truss structure," Engineering Structures, Vol. 207, 2020, p. 109932. https://doi.org/10.1016/j.engstruct.2019.109932

[20] Kraus, J. D., and Marhefka, R., Antennas for all applications, McGraw-Hill, 2002.

[21] Tan, L. T., and Pellegrino, S., "Thin-shell deployable reflectors with collapsible stiffeners Part 1: approach," AIAA Journal, Vol. 44, No. 11, 2006, pp. 2515–2523. https://doi.org/10.2514/1.16320

[22] Agrawal, P., Anderson, M., and Card, M., "Preliminary design of large reflectors with flat facets," IEEE Transactions on Antennas and Propagation, Vol. 29, No. 4, 1981, pp. 688–694. https://doi.org/10.1109/TAP.1981.1142631

[23] Shi, H., Yuan, S. and Yang, B., "New methodology of surface mesh geometry design for deployable mesh reflectors," Journal of Spacecraft and Rockets, 55(2), 2018, pp. 266-281. https://doi.org/10.2514/1.A33867

[24] Calladine, C. R., "Buckminster Fuller's "tensegrity" structures and Clerk Maxwell's rules for the construction of stiff frames," International Journal of Solids and Structures, Vol. 14, No. 2, 1978, pp. 161–172. https://doi.org/10.1016/0020-7683(78)90052-5

[25] Pellegrino, S., "Structural computations with the singular value decomposition of the equilibrium matrix," International Journal of Solids and Structures, Vol. 30, No. 21, 1993, pp. 3025–3035. https://doi.org/10.1016/0020-7683(93)90210-X

[26] Miura, K., and Pellegrino, S., Forms and Concepts for Lightweight Structures, Cambridge University Press, 2020. https://doi.org/10.1017/9781139048569

[27] Tibert, A., and Pellegrino, S., "Deployable tensegrity reflectors for small satellites," Journal of Spacecraft and Rockets, Vol. 39, No. 5, 2002, pp. 701–709. https://doi.org/10.2514/2.3867

[28] M55J High modulus carbon fiber, Toray Composite Materials America, Inc., 2020.

[29] Falcon User's Guide, SpaceX, September 2021.

[30] Starship Users Guide, SpaceX, March 2020.

[31] Suh, J.-E., Dassanayake, S., Thomson, M. and Pellegrino, S., "Concept for in-space assembly of large reflector antennas", 41st ESA Antenna Workshop, ESTEC, 2023.

[32] Suh, J.-E. , Dassanayake, S.P., Thomson, M. and Pellegrino, S. "Scalable concept for reflector antenna assembled in space", AIAA 2024 SciTech Forum, AIAA 2024-0823. https://doi.org/10.2514/6.2024-0823